ChemEngineering

MDPI

Article

Phase-Engineered P2/O3 Biphasic Sodium Cathodes via Mg Doping Without Na-Content Tuning

Sungmin Na [1], Hyunjin An [1] and Kwangjin Park [1,2,3,*]

[1] Department of Mechanical Engineering, Gachon University, 1342 Seongnamdaero, Sujeong-gu, Seongnam-si 13120, Republic of Korea; nasum621@gachon.ac.kr (S.N.); wlsgus@gachon.ac.kr (H.A.)
[2] Department of Battery Engineering, Gachon University, 1342 Seongnamdaero, Sujeong-gu, Seongnam-si 13120, Republic of Korea
[3] Koulomb, 1342 Seongnamdaero, Sujeong-gu, Seongnam-si 13120, Republic of Korea
* Correspondence: ydmj79@gachon.ac.kr

Abstract

Layered sodium transition-metal oxides are promising cathode materials for sodium-ion batteries due to their high theoretical capacity; however, their practical application is often limited by sluggish Na^+ diffusion kinetics and structural instability during cycling. P2/O3 phase coexistence has been proposed as an effective strategy to balance capacity and stability, yet it is typically achieved through precise Na-content tuning or complex synthesis conditions, which restrict compositional flexibility. Herein, we demonstrate a phase-engineering approach that induces stable P2/O3 phase coexistence without adjusting the overall Na stoichiometry by controlling the dopant incorporation pathway. Using $Na_{0.8}(Ni_{0.25}Fe_{0.33}Mn_{0.33}Cu_{0.07})O_2$ (NaNFMC) as a model system, Mg doping via a wet chemical route enables homogeneous dopant distribution, which triggers local stacking rearrangement and the formation of prismatic Na^+ diffusion channels characteristic of the P2 phase. In contrast, dry-doped samples with identical Mg content retain a predominantly O3-type structure, highlighting the decisive role of dopant incorporation in governing phase evolution. As a result of the phase-engineered P2/O3 coexisting framework, the Mg wet-doped cathode exhibits enhanced initial reversibility, superior rate capability, and improved long-term cycling stability compared to pristine and dry-doped counterparts. Voltage-resolved dQ/dV and cyclic voltammetry analyses reveal stabilized redox behavior with reduced polarization, while electrochemical impedance spectroscopy confirms suppressed impedance growth and improved Na^+ transport kinetics after cycling. This study establishes that phase engineering through controlled dopant incorporation provides an effective alternative to conventional Na-content tuning strategies for layered sodium cathodes. The findings offer a scalable and versatile design principle for optimizing the electrochemical performance and structural durability of next-generation sodium-ion battery cathode materials.

Keywords: sodium-ion battery; layered transition-metal oxides; P2/O3 phase; Mg doping; structural stability

Check for updates

Academic Editor: Evangelos Tsotsas

Received: 28 February 2026
Revised: 31 March 2026
Accepted: 8 April 2026
Published: 14 April 2026

Copyright: © 2026 by the authors. Licensee MDPI, Basel, Switzerland. This article is an open access article distributed under the terms and conditions of the Creative Commons Attribution (CC BY) license.

1. Introduction

Sodium-ion batteries (SIBs) have emerged as a promising alternative to lithium-ion batteries for large-scale energy storage applications, driven by the natural abundance, low cost, and geographical accessibility of sodium resources [1–7]. Despite these advantages,

the development of high-performance SIB cathodes remains challenging due to the intrinsically larger ionic radius of Na^+ (1.02 Å) compared to Li^+ (0.76 Å), which often leads to sluggish ion diffusion kinetics and pronounced structural instability during repeated cycling. Overcoming these limitations requires cathode materials that can simultaneously provide high reversible capacity, fast Na^+ transport, and long-term structural robustness. Layered transition-metal oxides with the general formula Na_xMO_2 (M = Ni, Fe, Mn, Co, Cu, etc.) are among the most extensively studied SIB cathodes, owing to their high theoretical capacity and structural similarity to layered lithium cathodes [8–11]. Depending on the oxygen stacking sequence and the coordination environment of Na^+ ions, these materials are commonly classified into P2-type and O3-type structures [12–14]. P2-type layered oxides possess prismatic Na^+ sites and exhibit rapid Na^+ diffusion and superior cycling stability; however, their relatively low Na content (typically $x \approx 0.67$) limits the achievable capacity [15–19]. In contrast, O3-type structures accommodate a higher Na content and thus offer higher theoretical capacity, but suffer from sluggish Na^+ diffusion, severe lattice strain, and irreversible phase transitions upon deep de-sodiation [5,6,18]. To integrate the complementary advantages of P2- and O3-type structures, P2/O3 coexisting layered oxides have recently attracted increasing attention as a promising cathode design strategy. The coexistence of prismatic and octahedral Na^+ sites can buffer lattice strain, mitigate irreversible phase transitions, and stabilize oxygen redox activity at high voltages, thereby improving cycling stability and rate capability [6]. However, most previously reported P2/O3 biphasic systems rely on precise control of the Na content or high-temperature synthesis to induce phase coexistence. Such approaches inherently limit compositional flexibility and complicate scalable material design, leaving open the question of whether phase coexistence can be achieved through alternative structural control strategies without adjusting the overall Na stoichiometry. Cation doping has been widely employed to enhance the structural stability of layered sodium cathodes, particularly in Fe/Mn-based systems where Jahn–Teller distortion associated with Mn^{3+} often accelerates lattice degradation [5,7,11,12,15].

Dopants such as Ti, Zr, Mg, Ca, and Cu have been shown to suppress structural deformation and improve cycling stability to varying degrees. Nevertheless, doping has generally been regarded as a means of local structural stabilization, while its potential role as a trigger for phase engineering, specifically the induction of controlled P2/O3 phase coexistence, has remained largely unexplored. In particular, Mg^{2+} is an electrochemically inert dopant with a stable electronic configuration and a relatively large ionic radius, making it effective in suppressing Jahn–Teller distortion and stabilizing transition-metal oxygen frameworks. Importantly, beyond dopant selection, the dopant incorporation pathway itself can play a critical role in governing local structural evolution and phase behavior in layered sodium cathodes. This highlights the possibility that the phase behavior of layered sodium cathodes can be engineered not through compositional tuning, but by controlling the dopant incorporation process itself.

Herein, we report a phase-engineered $Na_{0.8}(Ni_{0.25}Fe_{0.33}Mn_{0.33}Cu_{0.07})O_2$ (NaNFMC) layered cathode in which a stable P2/O3 biphasic structure is induced solely through Mg doping via a wet chemical route, without altering the overall Na content. Although identical Mg contents were employed, only the wet-doped sample exhibits homogeneous Mg incorporation at the atomic scale, leading to partial rearrangement of oxygen stacking and the formation of prismatic Na^+ diffusion channels characteristic of the P2 phase. As a result, the P2/O3 coexisting structure simultaneously delivers high reversible capacity, enhanced Na^+ diffusion kinetics, and improved cycling stability. Through comprehensive structural, electrochemical, and kinetic analyses, this work demonstrates that doping-mediated phase engineering rather than stoichiometric Na tuning offers an effective pathway to optimize layered sodium cathodes. The findings provide new insights into the interplay between

dopant distribution, phase coexistence, and electrochemical performance, and establish a scalable design principle for next-generation high-performance SIB cathodes.

2. Experimental

2.1. Synthesis of Cathode Material

$Ni_{0.25}Fe_{0.33}Mn_{0.33}Cu_{0.07}(OH)_2$ (Reshine New Material Co., Ltd., Nantong, China) was used as the precursor for synthesizing $Na_{0.8}Ni_{0.25}Fe_{0.33}Mn_{0.33}Cu_{0.07}O_2$ (NaNFMC Pristine). The precursor and 0.8 mol of NaOH were mixed using a planetary mill for 3 min, with the process repeated three times. The resulting mixture was sintered in an air atmosphere at 500 °C for 4 h, followed by 12 h at 900 °C, with heating and cooling rates of 2 °C/min. The final product was cooled to 250 °C to obtain NaNFMC Pristine. To synthesize Mg-doped NaNFMC, the precursor was mixed with NaOH and 0.01 mol of $Mg(OH)_2$, following the same sintering process as NaNFMC Pristine. Two doping methods, dry and wet, were employed as follows.

2.1.1. Dry Doping Method

$Mg(OH)_2$ was added to the precursor and mixed manually using a hand mixer for seven cycles. NaOH was then added and further mixed using a planetary mill for 3 min, repeated three times. The resulting mixture was sintered following the same conditions as the NaNFMC Pristine synthesis. The final product was referred to as NaNFMC Mg Dry Doping ($Na_{0.8}Ni_{0.25}Fe_{0.33}Mn_{0.33}Cu_{0.07}Mg_{0.01}O_2$).

2.1.2. Wet Doping Method

NaOH was dissolved in 80 mL of deionized water (DI water) at 60 °C with stirring for 5 min. The precursor was then added, followed by stirring for an additional 5 min. $Mg(OH)_2$ was subsequently added and stirred for another 5 min. The mixture was dried in an oven at 120 °C, and the dried powder was mixed using a planetary mill for 3 min, repeated three times. The powder was then sintered under the same conditions as the NaNFMC Pristine synthesis. The resulting product was referred to as NaNFMC Mg Wet Doping ($Na_{0.8}$ $Ni_{0.25}Fe_{0.33}Mn_{0.33}Cu_{0.07}Mg_{0.01}O_2$).

2.2. Materials Characteristics

The elemental compositions in each sample were determined using an Inductively Coupled Plasma Optical Emission System (ICP-OES) with a AVIO550 (Perkin Elmer, Waltham, MA, USA). The crystal structure of the Na^+ ion cathode materials were determined by X-ray diffraction (XRD) with a MiniFlex 600 XRD (Rigaku, a CuKα radiation source, Tokyo, Japan) in the 2θ range of 10–70°. Lattice parameters were obtained by Rietveld refinement with the SmartLab Studio II software package (SmartLab Studio II v4.4). Scanning Electron Microscopy (SEM) was performed on a SNE-4500M plus (Sec, Suwon, Republic of Korea), and Energy Dispersive Spectrometer (EDS) mapping was performed on a XFlash 630 Mini (Bruker, Billerica, MA, USA).

2.3. Electrochemical Measurement of Coin Half Cell

The electrochemical properties were tested using an R2032-type coin cell (Wellcos, Gunpo-si, Republic of Korea) with a Na-metal anode. Composite electrodes containing 80 wt.% active materials, 10 wt.% conductive carbon (Denka black), and a 10 wt.% polyvinylidene fluoride (PVdF) binder were cast on 20 μm aluminum foil and were then used as current collectors, with an active material loading level of approximately 2 mg cm^{-2} (±3%). The electrodes were dried at 120 °C in an oven and pressed until the electrode density was 1.5 mg cm^{-3} (±3%). The electrolyte used was 1 mol L^{-1} of $NaPF_6$

dissolved in a mixture of ethylene carbonate and diethylene carbonate (EC:PC = 1:1). The R2032-type coin cells were lastly assembled in a glove box under an argon atmosphere. Galvanostatic cycling tests were performed with a cycler (CT3001A, Landt, Vestal, NY, USA) in a temperature chamber at room temperature. For the Cyclic Voltammetry (CV) measurements, the cells were measured with different scan rates at each 0.1, 0.2, 1 and 2 mV/s between 2.0 and 4.3 V. Electrochemical Impedance Spectroscopy (EIS) was measured at an open-circuit potential using an electrochemical analyzer (Vertex one, HS tech, Seongnam-si, Republic of Korea) in the 10 μHz-to-250 kHz range to scan rate.

3. Results and Discussion

Table 1 summarizes the elemental compositions of $Na_{0.8}(Ni_{0.25}Fe_{0.33}Mn_{0.33}Cu_{0.07}Mg_{0.01})O_2$ (NaNFMC Pristine), and Mg-doped NaNFMC samples prepared via dry and wet doping methods. Inductively coupled plasma optical emission spectroscopy (ICP-OES) confirms that all samples closely match their targeted compositions, with nearly identical Mg contents in both dry- and wet-doped samples. This compositional consistency eliminates stoichiometric variation as a governing factor and indicates that the observed differences in structural evolution and electrochemical behavior originate primarily from the dopant incorporation pathway.

Table 1. Elemental compositions for NaNFMC Pristine, NaNFMC Mg dry doping, and NaNFMC Mg wet doping obtained from ICP-OES measurements.

Targeted Chemical Formula	Measured Molar Ratio						
	Na	Ni	Fe	Mn	Cu	Mg	O
NaNFMC Pristine	0.8	0.3412	0.4264	0.4457	0.0998	-	2.1893
NaNFMC Mg dry doping	0.8	0.3193	0.4081	0.4192	0.0949	0.0169	1.8212
NaNFMC Mg wet doping	0.8	0.3529	0.4432	0.4654	0.1008	0.0155	1.3112

Scanning electron microscopy (SEM) images (Figure 1a–c) show that all samples exhibit similar plate-like morphologies with particle sizes in the range of 2–5 μm, suggesting that Mg doping does not significantly alter the macroscopic particle morphology. However, a clear distinction emerges from elemental distribution analysis using energy-dispersive X-ray spectroscopy (EDS). As shown in Figure 1, the wet-doped sample exhibits a homogeneous Mg distribution throughout the secondary particles, whereas the dry-doped sample shows localized Mg enrichment, indicative of incomplete diffusion during the solid-state mixing and sintering process. Such differences in dopant distribution are particularly critical in layered sodium transition-metal oxides, where local cation inhomogeneity can strongly influence oxygen stacking stability and Na^+ coordination environments. Homogeneous Mg incorporation is expected to alleviate local strain heterogeneity and promote cooperative gliding of oxygen layers, which is a prerequisite for the formation of prismatic Na^+ sites characteristic of the P2 structure. In contrast, localized Mg aggregation may hinder stacking rearrangement and preserve the original octahedral Na^+ coordination, thereby stabilizing the O3-type framework. These observations suggest that the dopant incorporation pathway plays a decisive role in determining the subsequent phase evolution.

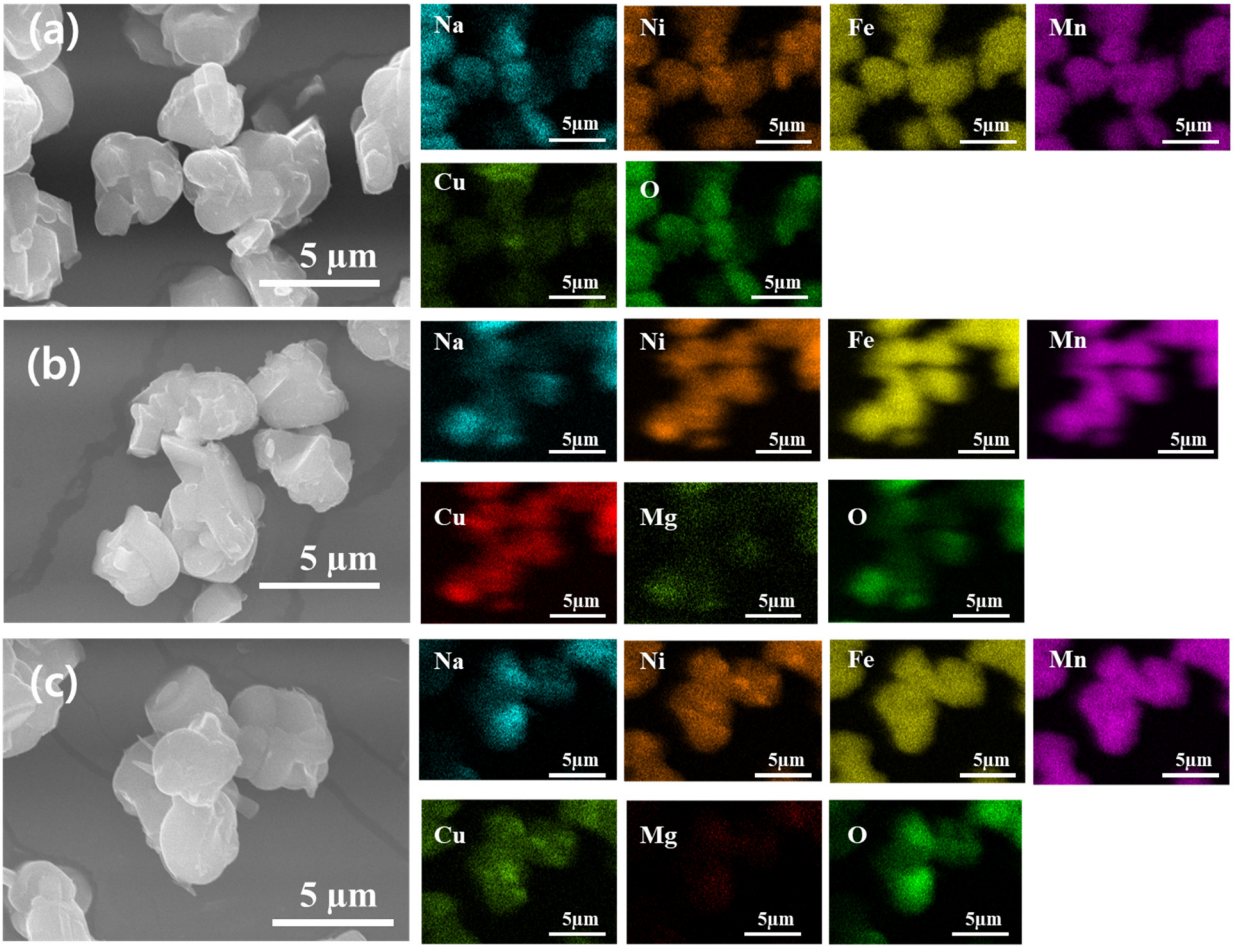

Figure 1. SEM images and EDS mapping results. (**a**) NaNFMC Pristine, (**b**) NaNFMC Mg dry doping, and (**c**) NaNFMC Mg wet doping.

The influence of dopant distribution on crystal structure is directly reflected in the X-ray diffraction (XRD) patterns shown in Figure 2a. All samples crystallize in the layered α-$NaFeO_2$-type structure (space group $R\bar{3}m$, JCPDS No. 54-0887) [2,4,18]. However, magnified views of the diffraction region between 15.5° and 16.5° revesal pronounced differences in phase composition. Both the NaNFMC Pristine and Mg dry-doped samples predominantly display the (003) reflection associated with the O3-type structure, before and after the formation cycle. In contrast, the Mg wet-doped sample exhibits two distinct reflections corresponding to the (002) plane of the P2 phase and the (003) plane of the O3 phase, demonstrating the formation of a stable P2/O3 coexisting structure. Importantly, this phase coexistence is achieved without altering the overall Na stoichiometry, distinguishing the present approach from previously reported P2/O3 biphasic systems that rely on Na-deficient compositions or high-temperature phase separation. The result highlights that controlled dopant incorporation alone can serve as an effective trigger for phase engineering in layered sodium cathodes. Furthermore, the (003) peak of the wet-doped sample shifts toward lower 2θ values after cycling, indicating lattice expansion associated with effective Mg^{2+} substitution within the transition-metal layers. This behavior is not observed in the dry-doped sample, underscoring that homogeneous Mg incorporation is essential for inducing stacking rearrangement from the O3-type ABCABC oxygen stacking to the P2-type ABBA configuration [18,19].

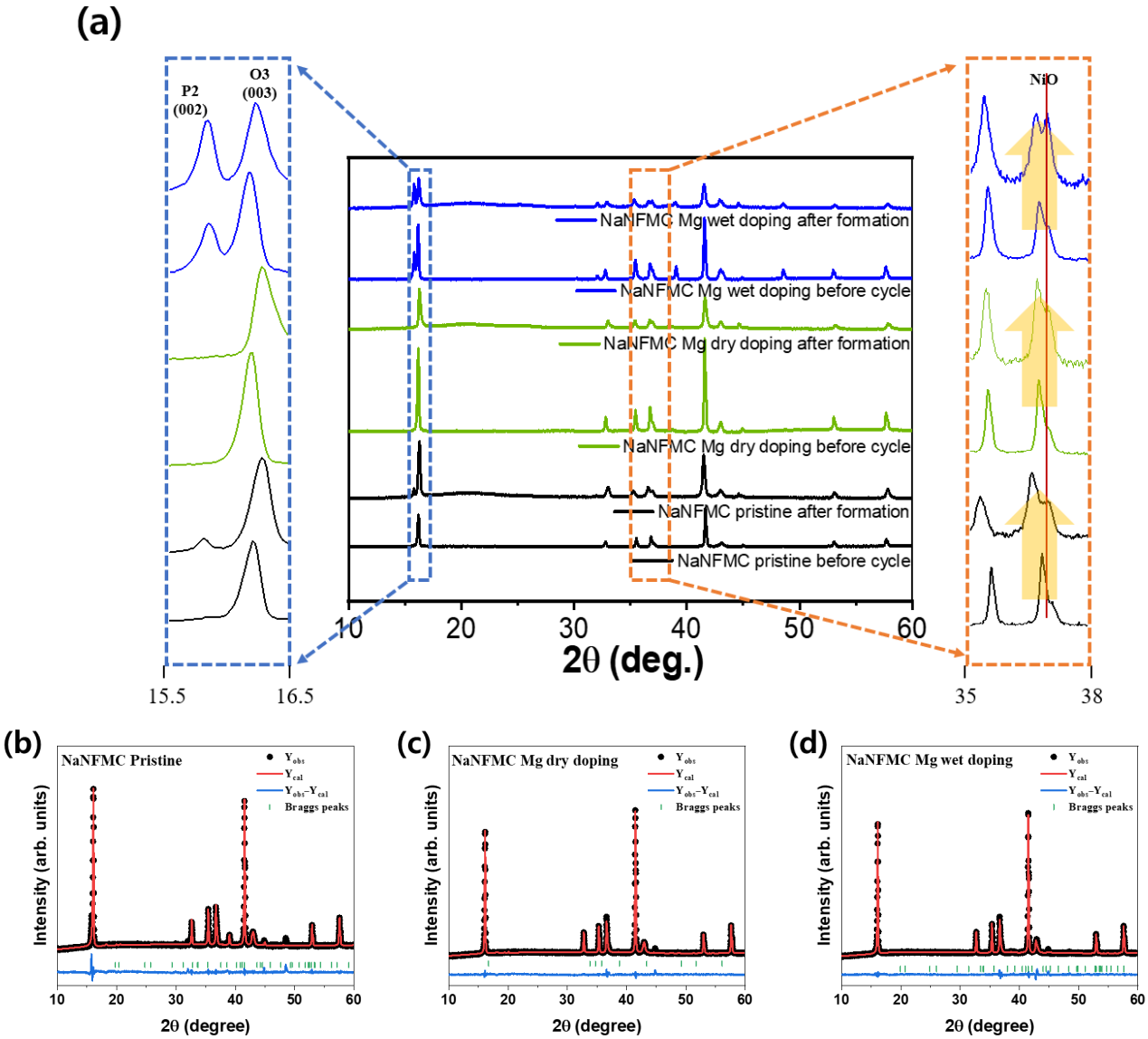

Figure 2. (**a**) X-ray diffraction (XRD) patterns of pristine, Mg dry-doped, and Mg wet-doped NaNFMC samples before and after formation. The magnified regions highlight the characteristic reflections of P2 (002) and O3 (003) phases (**left**) and the presence of a weak NiO-related peak (**right**). The wet-doped sample exhibits features corresponding to a biphasic P2/O3 structure, whereas the pristine and dry-doped samples primarily retain the O3-type structure. The slight peak shifts observed after formation indicate structural evolution during electrochemical cycling. (**b**–**d**) Rietveld refinement profiles of (**b**) pristine, (**c**) Mg dry-doped, and (**d**) Mg wet-doped samples. The observed (black dots), calculated (red line), and difference (blue line) patterns are shown along with the Bragg peak positions (green ticks). The wet-doped sample was refined using a two-phase model consisting of P2 and O3 phases, confirming the formation of a biphasic structure induced by homogeneous Mg incorporation.

Rietveld refinement was performed to further elucidate the structural origin of the phase coexistence (Figure 2b–d and Table 2). The Rietveld refinement of the Mg wet-doped sample was performed using a two-phase model consisting of P2 and O3 phases. The corresponding Bragg peak positions for each phase are separately indicated, showing good agreement with the experimental diffraction. Compared with the pristine and dry-doped samples, the wet-doped NaNFMC exhibits more pronounced changes in lattice parameters, consistent with partial substitution of Mn^{4+} by larger Mg^{2+} ions. The resulting local lattice distortion facilitates oxygen-layer gliding and stabilizes prismatic Na^{+} sites,

enabling the coexistence of P2 and O3 domains within a single composition. These results indicate that Mg wet doping plays a role beyond simple structural stabilization by promoting stacking rearrangement and enabling the formation of a P2/O3 coexisting framework. The emergence of prismatic Na^+ diffusion channels within the P2/O3 coexisting framework is expected to exert a significant influence on Na^+ transport kinetics and redox reversibility [2,4,11,16,17,20]. In particular, the coexistence of prismatic and octahedral Na^+ sites can provide complementary diffusion pathways while mitigating lattice strain during repeated Na^+ insertion and extraction. The electrochemical consequences of this phase-engineered structure are examined in detail in the following section.

Table 2. Summary of R factors and lattice parameters from Rietveld refinements for all the samples.

Samples	R Factors and Lattice Parameters						
	a [Å]	b [Å]	c [Å]	V [Å^3]	c/a	Rwp	Rp
NaNFMC Pristine	5.7314	7.1845	5.4578	224.737	0.952	5.6%	3.5%
NaNFMC Mg dry doping	5.6875	7.1453	5.3517	217.486	0.941	3.96%	2.67%
NaNFMC Mg wet doping	5.6671	7.1737	5.3817	218.789	0.950	3.80%	2.78%

Figure 3a presents the initial charge–discharge profiles of the NaNFMC Pristine, Mg dry-doped, and Mg wet-doped samples measured at 0.05 C within a voltage range of 2.0–4.2 V. All samples exhibit characteristic sloping voltage profiles associated with transition-metal redox reactions, followed by a high-voltage region related to anionic redox activity. Notably, the Mg wet-doped sample delivers a higher initial discharge capacity and shows a smoother voltage evolution compared to the pristine and dry-doped samples. This behavior indicates more reversible Na^+ insertion and extraction from the initial cycle, suggesting that the phase-engineered P2/O3 coexisting structure provides a more stable electrochemical reaction environment. The stabilized voltage response of the Mg wet-doped electrode can be attributed to the structural buffering effect arising from the coexistence of P2 and O3 phases. In particular, the presence of prismatic Na^+ sites in the P2 domains is expected to accommodate local lattice distortion during Na^+ extraction at high states of charge, thereby mitigating abrupt stacking rearrangements typically observed in single-phase O3-type cathodes. As a result, the phase-engineered cathode maintains a more gradual and continuous electrochemical response during the initial activation process [21,22]. Further insight into the redox behavior is provided by the differential capacity (dQ/dV) curves shown in Figure 4d–f. The pristine and Mg dry-doped samples exhibit pronounced peak broadening and noticeable peak shifts upon cycling, indicative of increasing polarization and irreversible phase evolution [2,22]. In contrast, the Mg wet-doped sample maintains sharper and more symmetric redox peaks with minimal potential shifts over repeated cycles. Such behavior reflects enhanced redox reversibility and suppressed structural rearrangement, consistent with the stabilizing effect of the P2/O3 coexisting framework [2,3,21,23]. As such, all samples containing NaNFMC exhibit distinct plateaus during charge/discharge cycling, with the contributions of Mn and Ni clearly evident in the plateau regions observed during galvanostatic cycling. This characteristic shape of the charge/discharge curve indicates that Mg doping introduces minimal disruption to the electrochemical reaction process, preserving the structural integrity and reversibility of the redox reactions. This further suggests that Mg incorporation is highly compatible with the electrochemical mechanisms of the material. The initial reversible discharge capacities are 135.46, 136.06, and 141.04 mAh/g at NaNFMC Pristine, NaNFMC Mg dry doping, and NaNFMC wet doping samples, respectively. The rate performance of all samples with

different current rates (0.2, 0.33, 0.5, 1 and 2 C) are shown in Figure 3b. The C-rate discharge capacity ratio of 2/0.2 C was 80.9, 79.9, and 81.8% at NaNFMC Pristine, NaNFMC Mg dry doping and NaNFMC Mg wet doping, showing the best C-rate efficiency in the NaNFMC Mg wet doping. Even at the high rates of 2 C, the NaNFMC Mg wet doping samples can still deliver 104.35 mAh/g. As can be seen from the XRD peaks in Figure 2, the NaNFMC Mg wet doping sample in which the P2 phase and the O3 phase exist appropriately showed more discharge capacity as well as excellent rate capability compared to the NaNFMC Mg dry doping sample with more of an O3 phase structure. This might be because Na^+ ions can move relatively more easily in a P2-type structure with a Prismatic structure than an O3-type structure with an Octahedra structure with the same amount of Na mol [6,24]. The inferior rate capability of the dry-doped sample is attributed to the inhomogeneous distribution of Mg, which can locally disrupt Na^+ diffusion pathways and increase kinetic resistance, resulting in sluggish electrochemical kinetics. The cycling performances were tested at 0.5 C for 100 cycles shown in Figure 3c. The NaNFMC Pristine, NaNFMC Mg dry doping and NaNFMC Mg wet doping exhibits 73.8, 66.05, and 72.7% of cycle retention at the 100th cycle in the voltage window of 2.0–4.3 V. Although both Mg-doped samples exhibit comparable long-term cycling stability, the wet-doped sample demonstrates improved initial reversibility and rate capability, indicating enhanced reaction kinetics at early stages. As shown in Figure 2, since the NaNFMC Mg dry doping sample has a complete O3-type structure, the active material with a structurally weak O3-type structure has a phase change as charging and discharging cycles are repeated, resulting in rapid electrochemical performance degradation. However, it is thought that high cycling retention and excellent rate capability were secured by securing structural stability due to proper coexistence with a relatively stable P2-type structure. This difference in electrochemical performance seems to be attributed to stable oxygen redox with a coexisting structure of P2 and O3 phases. To further elucidate redox behavior, differential capacity (dQ/dV) profiles were collected at various cut-off voltages (Figure 4). At cut-off voltages below 4.1 V vs. Na/Na^+, dQ/dV show two reversible redox reactions occurring at around 3.1 V and 3.7 V with small polarizations (Figure 4d–f). These two non-polarization peaks are attributed to the conventional redox reactions of Mn and Ni. However, new polarization peaks appear in the cut-off voltage range of upper 3.9 V. These additional peaks are due to the redox reaction of oxygen [4,25]. At higher voltages (>3.9 V), oxygen redox features emerge. The wet-doped sample shows narrower, more symmetric peaks with reduced polarization across the voltage range, suggesting enhanced redox reversibility [4,26]. The suppression of Jahn–Teller distortion is critical in Mn-based cathodes. Mn^{3+} ions tend to distort MnO_6 octahedra, leading to lattice strain and phase instability. Incorporating Mg^{2+} into Mn sites not only reduces Mn^{3+} content but also eliminates JT-active sites due to its stable electronic configuration. This structural stabilization is reflected in the dQ/dV curves by minimized voltage hysteresis and maintained peak positions after cycling. The P2 domains likely further mitigate structural collapse by providing prismatic Na^+ pathways and buffering local lattice strain during Na^+ extraction/insertion [6,15,27].

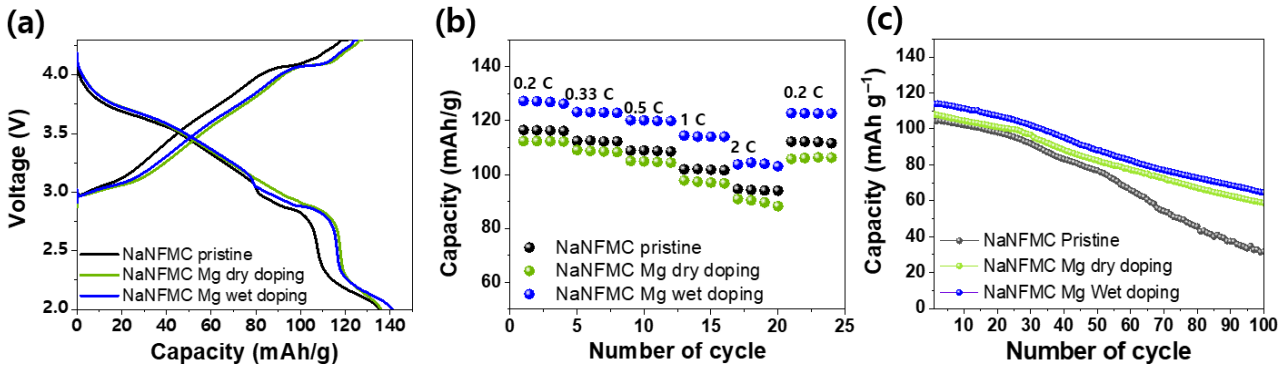

Figure 3. Electrochemical performances of NaNFMC. (**a**) Initial charge–discharge curves of the NaNFMC Pristine, NaNFMC Mg dry doping and NaNFMC Mg wet doping samples at 0.05 C in range 2.0–4.3 V at room temperature, (**b**) discharge cycling data of each sample at different discharge rates from 0.2 C to 3 C, (**c**) the cycle retention performance at room temperature in the voltage range of 2.0–4.3 V at 1 C rate.

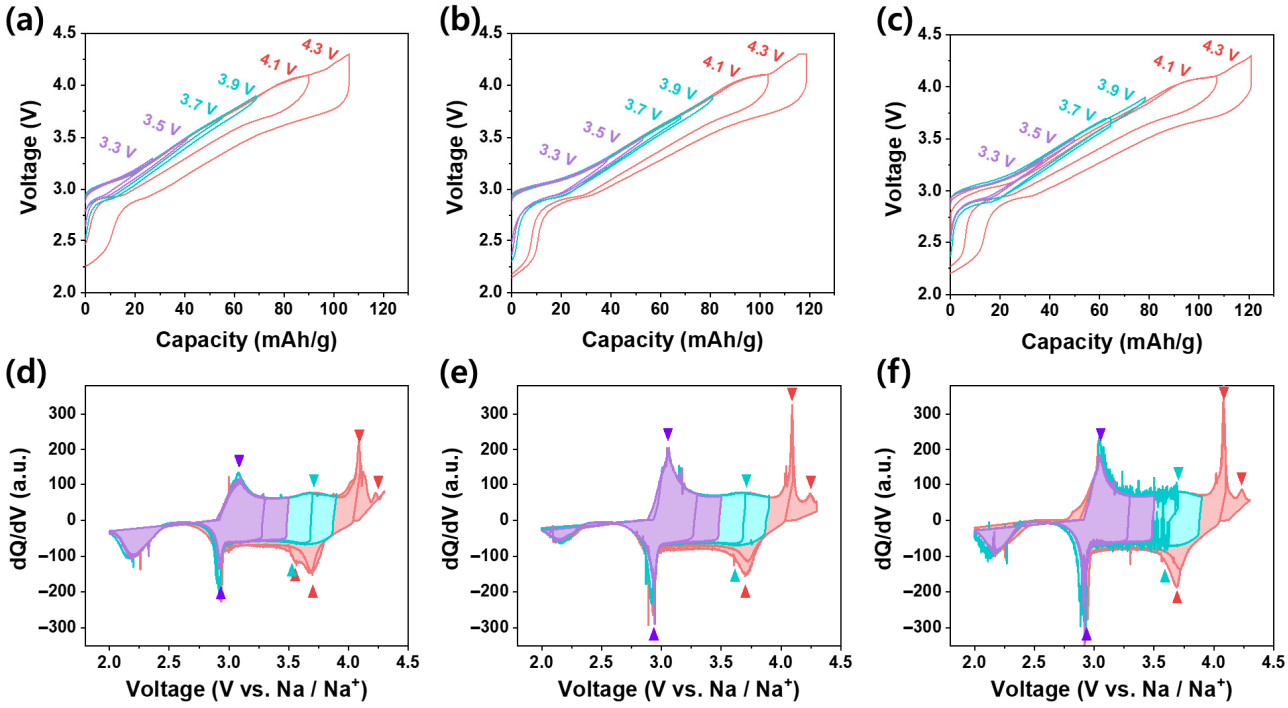

Figure 4. Galvanostatic charge/discharge curves and their dQ/dV plots at C/20 with increasing the upper cut-off voltage from 2.0 to 4.8 V vs. Na/Na^+. (**a**,**d**) Charge/discharge graph from 3.3 V to 4.3 V by increasing the cut-off voltage of the NaNFMC Pristine sample by 0.3 V and a dQ/dV plot, (**b**,**e**) NaNFMC Mg dry doping, and (**c**,**f**) NaNFMC Mg wet doping. The triangles in each dQ/dV plot represent reversible redox couples and the arrows indicate the coexistence of non-polarization and polarization redox couples. The arrows in (**d**–**f**) indicate the anodic and cathodic redox couples associated with transition-metal and oxygen redox reactions.

Cyclic voltammetry (CV) measurements at multiple scan rates (0.1, 0.2, 1 and 2 mV/s) between 2.0 and 4.3 V vs. Na^+/Na. follow a linear relationship between the peak current and the square root of the scan rate, indicating diffusion-controlled processes (Figure 5a–c) [1,4]. The apparent Na^+ diffusion coefficients can be calculated based on the following Randles–Sevcik Equation (1) [1,3,28].

$$I_p = 2.69 \times n^{3/2} A D^{1/2} v^{1/2} \Delta C_0 \quad (1)$$

where n is the number of electrons transferred in the redox reaction (for $Fe^{2+/3+}$ it is 1), A is the area of the electrolyte-locked cathode, D is the apparent Na^+ diffusion coefficient, and ΔC_0 is the change in the Na^+ concentration. In the upper equation, this means that the peak current (I_p) is proportional to the square root of the sweep rate ($v^{1/2}$), indicating that the process is extensively controlled. The slope of the linear fits for the charge/discharge process and the corresponding calculated D values are listed in Figure 5d [1,3,28]. The calculated Na^+ diffusion coefficient (via Randles–Sevcik equation) is 3.89×10^{-11}; for Pristine, the apparent Na^+ diffusion coefficient of NaNFMC Mg wet doping increased to 4.04×10^{-11}, respectively, which indicates better rate performance (Figure 5d). The order of magnitude for the Na^+ diffusion coefficients during oxidation and reduction remains comparable, indicating the prominent reversibility of Na^+ intercalation and de-intercalation processes [1,3,28]. However, in contrast to this behavior, the Mg dry-doped sample exhibits a lower Na^+ diffusion coefficient (3.62×10^{-11}) than even the NaNFMC Pristine sample. This reduced diffusion kinetics may be attributed to the inhomogeneous incorporation of Mg in the dry-doped sample, which can locally distort the layered framework and partially obstruct Na^+ diffusion pathways. In comparison, the Mg wet-doped sample shows a significantly higher Na^+ diffusion coefficient, confirming that homogeneous Mg incorporation and the resulting P2/O3 coexisting structure effectively enhance Na^+ transport kinetics. The coexistence of prismatic and octahedral Na^+ sites provides mixed diffusion pathways and reduces energy barriers for Na^+ migration, leading to improved diffusion behavior [24,29].

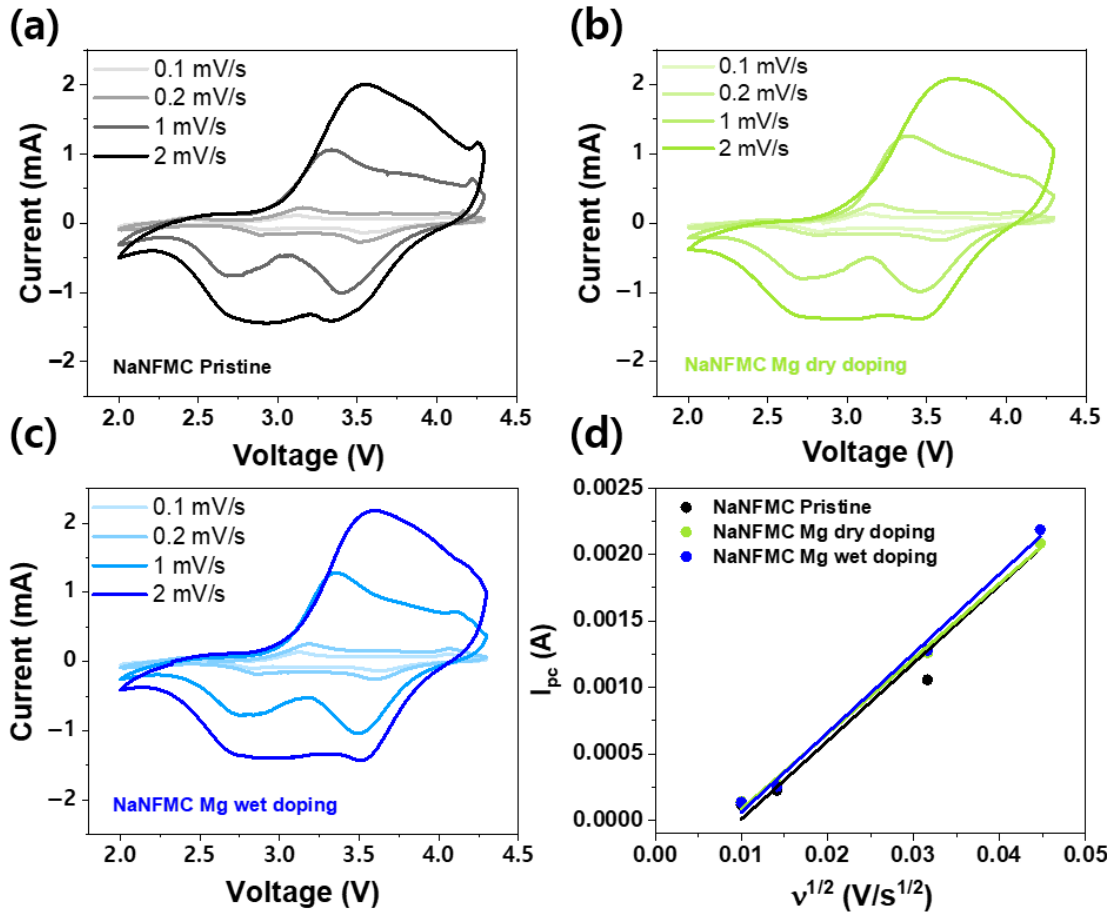

Figure 5. Cyclic Voltammetry (CV) profile at different scan rates of 0.1, 0.2, 1 and 2 mV/s between 2.0 and 4.3 V. (**a**) NaNFMC Pristine, (**b**) NaNFMC Mg dry doping, (**c**) NaNFMC Mg wet doping, and ion diffusion and (**d**) peak current in the function of square root of the scan rate.

To further investigate the resistance caused by the differences in structural change in the NaNFMC Pristine, NaNFMC Mg dry doping, and NaNFMC Mg wet doping samples, EIS analysis was performed after the 1st and 100th cycles at 0.5 C in the voltage range of 2.0–4.3 V and frequency ranging from 1 to 100 kHz, as shown in Figure 6a,b. Each generated impedance spectrum consists of three phase areas; first, the semicircle of the high-frequency area is related to the impedance of the Na-ion diffusion through the solid-electrolyte interface (SEI); second, the semi-circle of the medium frequency area indicates the charge interface capacitance and transfer resistance at the surface at the cathode–electrolyte interface; and finally, the sloping lines of the low-frequency area are related to the Warburg impedance, which represents the Na-ion diffusion inside the cathode [30–32]. When all impedance spectra are fitted to an equivalent circuit, R_S represents the resistance of the electrolyte, R_{SEI} represents the resistance of the SEI film, and the R_{CT} represents the charge transfer resistance, as shown in Table 3. Notably, the NaNFMC Mg wet doping sample, which maintains the P2/O3 coexisting structure well after cycling, showed the lowest charge transfer resistance increase rate. The improvement of structural stability and Na^+ diffusivity in the NaNFMC Mg wet doping sample effectively overcome the disadvantages of the O3 structure, which is structurally easy to collapse due to the appropriate substitution of Mg in the transition-metal layer, and it is confirmed that the coexisting formation with the P2 structure enables reversible Na^+ transport in the layered structure cathode materials. Taken together, the wet-doped NaNFMC sample demonstrates a well-balanced combination of high capacity, fast rate performance, and structural integrity. These benefits arise from the synergistic effect of a P2/O3 biphasic structure and uniform Mg incorporation, which collectively promote Na^+ transport and suppress irreversible degradation mechanisms. These findings reinforce the value of controlled phase coexistence in optimizing layered sodium cathodes for high-performance applications.

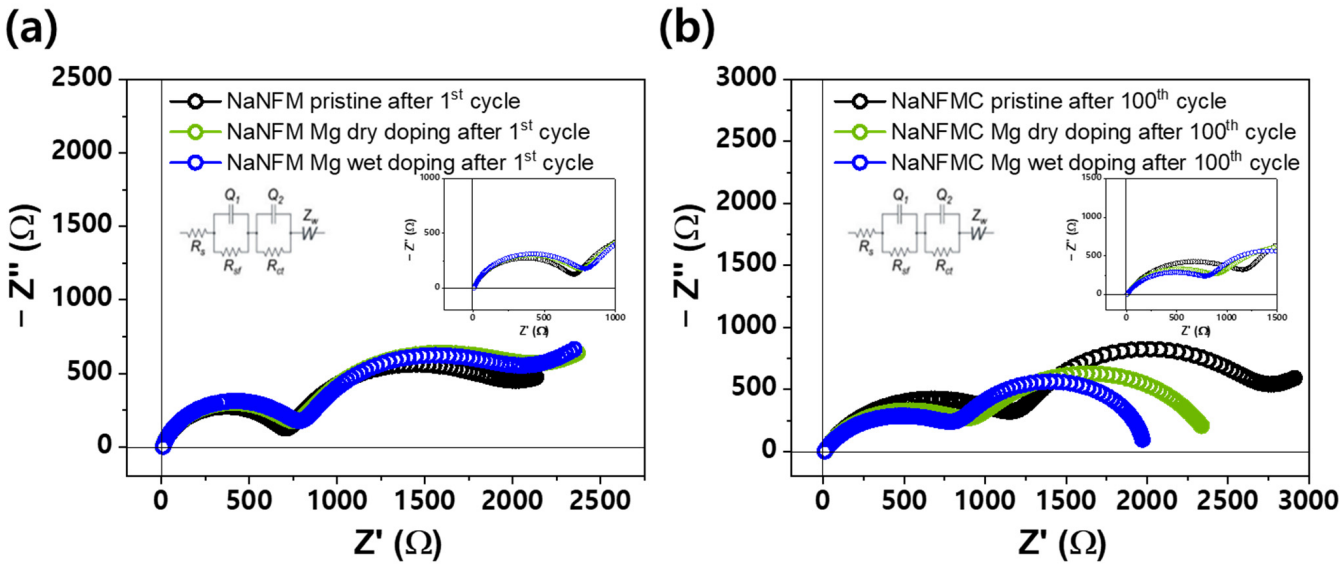

Figure 6. Impedance spectra of Pristine, dry-doped NaNFM and wet-doped NaNFM. (**a**) After initial cycle and (**b**) after 100th cycle.

Table 3. EIS-based R_S, R_{SEI} and R_{CT} values of the pristine and incipient samples at the 1st and 100th cycles in the Nyquist plots.

Samples	After 1st Cycle			After 100th Cycle		
	R_s	R_{SEI}	R_{CT}	R_s	R_{SEI}	R_{CT}
NaNFMC Pristine	7.428	694.7	1113	10.17	1233	1171
NaNFMC Mg dry doping	6.38	743.3	1126	10.27	1367	957.1
NaNFMC Mg wet doping	7.029	771.9	1011	7.314	1080	897

4. Conclusions

In this study, we demonstrated a phase-engineering strategy for layered sodium cathodes that enables stable P2/O3 phase coexistence without adjusting the overall Na stoichiometry. By employing Mg doping through a wet chemical route, homogeneous dopant incorporation was achieved, which effectively triggered local stacking rearrangement and induced the coexistence of prismatic and octahedral Na^+ coordination environments within a single $Na_{0.8}(Ni_{0.3}Fe_{0.4}Mn_{0.4}Cu_{0.1})O_2$ composition. Structural analyses revealed that, despite identical Mg contents, only the wet-doped sample exhibited uniform Mg distribution and a stable P2/O3 biphasic structure, whereas the dry-doped counterpart retained a predominantly O3-type framework. This result highlights that the dopant incorporation pathway, rather than compositional tuning, plays a decisive role in governing phase evolution in layered sodium transition-metal oxides. The induced phase coexistence provides a structural buffer that mitigates lattice strain and suppresses irreversible phase transitions during repeated Na^+ insertion and extraction. Electrochemical evaluation further confirmed the advantages of the phase-engineered cathode. The Mg wet-doped sample delivered enhanced initial reversibility, superior rate capability, and improved long-term cycling stability compared to pristine and dry-doped electrodes. Voltage-resolved dQ/dV and cyclic voltammetry analyses demonstrated stabilized redox behavior with reduced polarization, indicating a more homogeneous and reversible reaction environment enabled by the P2/O3 coexisting framework. In addition, electrochemical impedance spectroscopy revealed suppressed impedance growth and lower charge-transfer resistance after cycling, confirming improved Na^+ transport kinetics and interfacial stability. The key difference between dry and wet doping lies in the dopant distribution. While dry doping relies on mechanical mixing and may result in inhomogeneous Mg distribution, wet doping enables molecular-level mixing, leading to more uniform incorporation of Mg into the lattice. This homogeneous distribution promotes oxygen stacking rearrangement, resulting in the formation of a stable P2/O3 biphasic structure.

Collectively, these results establish that phase engineering via controlled dopant incorporation offers an effective alternative to conventional Na-content tuning strategies for optimizing layered sodium cathodes. By decoupling phase control from stoichiometric adjustment, the present approach provides greater compositional flexibility while simultaneously enhancing electrochemical performance and structural durability. This work thus presents a scalable and versatile design principle for developing high-performance layered cathode materials for next-generation sodium-ion batteries.

Author Contributions: Conceptualization, S.N. and K.P.; Methodology, S.N. and H.A.; Validation, H.A.; Resources, K.P.; Writing—original draft, S.N.; Supervision, K.P.; Project administration, K.P. All authors have read and agreed to the published version of the manuscript.

Funding: This work was supported by the Gachon University research fund of 2024 (GCU-202404200001).

Data Availability Statement: The original contributions presented in this study are included in the article. Further inquiries can be directed to the corresponding author.

Conflicts of Interest: Author Kwangjin Park was employed by the company Koulomb. The remaining authors declare that the research was conducted in the absence of any commercial or financial relationships that could be construed as a potential conflict of interest.

References

1. Yue, J.L.; Zhou, Y.N.; Yu, X.; Bak, S.M.; Yang, X.Q.; Fu, Z.W. Facile synthesis of porous Co–Fe layered double hydroxide nanosheet arrays on Ni foam for high-performance asymmetric supercapacitors. *J. Mater. Chem. A Mater.* **2015**, *3*, 23261. [CrossRef]
2. Zhang, C.; Gao, R.; Zheng, L.; Hao, Y.; Liu, X. New Insights into the Roles of Mg in Improving the Rate Capability and Cycling Stability of O3-$NaMn_{0.48}Ni_{0.2}Fe_{0.3}Mg_{0.02}O_2$ for Sodium-Ion Batteries. *ACS Appl. Mater. Interfaces* **2018**, *10*, 10819–10827. [CrossRef]
3. Mao, Q.; Zhang, C.; Yang, W.; Yang, J.; Sun, L.; Hao, Y.; Liu, X. Facile fabrication of novel 3D flower-like Mn–Co sulfide architectures supported on Ni foam for high-performance hybrid supercapacitors. *J. Alloys Compd.* **2019**, *794*, 509. [CrossRef]
4. Qi, X.; Liu, L.; Song, N.; Gao, F.; Yang, K.; Lu, Y.; Yang, H.; Hu, Y.S.; Cheng, Z.H.; Chen, L. In Situ Fabrication of Honeycomb-Like Carbon Nanotubes/Graphene Microspheres as High-Performance Anode Materials for Sodium-Ion Batteries. *ACS Appl. Mater. Interfaces* **2017**, *9*, 40215. [CrossRef]
5. Tapia-Ruiz, N.; Armstrong, A.R.; Alptekin, H.; Amores, M.A.; Au, H.; Barker, J.; Boston, R.; Brant, W.R.; Brittain, J.M.; Chen, Y.; et al. 2021 roadmap for sodium-ion batteries. *J. Phys. Energy* **2021**, *3*, 031503. [CrossRef]
6. Liang, X.; Sun, Y.K. A Novel Pentanary Metal Oxide Cathode with P2/O3 Biphasic Structure for High-Performance Sodium-Ion Batteries. *Adv. Funct. Mater.* **2022**, *32*, 2206154. [CrossRef]
7. Fang, Y.; Xiao, L.; Chen, Z.; Ai, X.; Cao, Y.; Yang, H. Recent Progress in High-Temperature Sodium-Ion Batteries: Key Materials and Optimization Strategies. *Electrochem. Energy Rev.* **2018**, *1*, 294. [CrossRef]
8. Zheng, Y.M.; Huang, X.B.; Meng, X.M.; Xu, S.D.; Chen, L.; Liu, S.B.; Zhang, D. N-Doped Carbon Nanotubes Grafted on MXene as High-Performance Anodes for Lithium-Ion Batteries. *ACS Appl. Mater. Interfaces* **2021**, *13*, 45528. [CrossRef]
9. Oh, S.M.; Myung, S.T.; Yoon, C.S.; Lu, J.; Hassoun, J.; Scrosati, B.; Amine, K.; Sun, Y.K. Highly Cyclable Lithium–Sulfur Batteries with a Dual-Type Sulfur Cathode and a Lithiated Si/SiOx Nanosphere Anode. *Nano Lett.* **2014**, *14*, 1620. [CrossRef]
10. Wang, P.F.; You, Y.; Yin, Y.X.; Guo, Y.G. A Flexible and Robust Silicon/Carbon/Graphite Composite Paper for Advanced Lithium-Ion Batteries. *J. Mater. Chem. A Mater.* **2016**, *4*, 17660. [CrossRef]
11. Kim, S.; Min, K.; Park, K. Y-doped P2-type $Na_{0.67}Ni_{0.33}Mn_{0.67}O_2$: A sodium-ion battery cathode with fast charging and enhanced cyclic performance. *J. Alloys Compd.* **2021**, *874*, 160027. [CrossRef]
12. Xie, Y.; Gabriel, E.; Fan, L.; Hwang, I.; Li, X.; Zhu, H.; Ren, Y.; Sun, C.; Pipkin, J.; Dustin, M.; et al. Role of Lithium Doping in P2-$Na_{0.67}Ni_{0.33}Mn_{0.67}O_2$ for Sodium-Ion Batteries. *Chem. Mater.* **2021**, *33*, 4445. [CrossRef]
13. Delmas, C.; Fouassier, C.; Hagenmuller, P. Structural classification and properties of the layered oxides. *Phys. B+C* **1980**, *99*, 81–85. [CrossRef]
14. Wang, H.; Gu, M.; Jiang, J.; Lai, C.; Ai, X. An O3-type $NaNi_{0.5}Mn_{0.3}Ti_{0.2}O_2$ compound as new cathode material for room-temperature sodium-ion batteries. *J. Power Sources* **2016**, *327*, 653–657. [CrossRef]
15. Singh, G.; Tapia-Ruiz, N.; Del Amo, J.M.L.; Maitra, U.; Somerville, J.W.; Armstrong, A.R.; De Ilarduya, J.M.; Rojo, T.; Bruce, P.G. Understanding the Role of Carbon Coating in Enhancing the Electrochemical Performance of Na_2FePO_4F for Sodium-Ion Batteries. *Chem. Mater.* **2016**, *28*, 5087. [CrossRef]
16. Wu, X.; Guo, J.; Wang, D.; Zhong, G.; McDonald, M.J.; Yang, Y. Advanced Electrolyte Additives for Improving the Cycling Stability of High-Voltage $LiNi_{0.5}Co_{0.2}Mn_{0.3}O_2$ Cathodes in Lithium-Ion Batteries. *J. Power Sources* **2015**, *281*, 18. [CrossRef]
17. Han, M.H.; Gonzalo, E.; Singh, G.; Rojo, T. Recent Advances and Perspectives on Layered Oxide Cathodes for Sodium-Ion Batteries. *Energy Environ. Sci.* **2015**, *8*, 81. [CrossRef]
18. Jung, K.N.; Choi, J.Y.; Shin, H.S.; Huu, H.T.; Im, W.B.; Lee, J.W. Mg-doped $Na[Ni_{1/3}Fe_{1/3}Mn_{1/3}]O_2$ with enhanced cycle stability as a cathode material for sodium-ion batteries. *Solid. State Sci.* **2020**, *106*, 106334. [CrossRef]
19. Liu, G.; Xu, W.; Wu, J.; Li, Y.; Chen, L.; Li, S.; Ren, Q.; Wang, J. 3D porous $Na_3V_2(PO_4)_3$/C composite as high-performance cathode for sodium-ion batteries. *J. Energy Chem.* **2023**, *83*, 53. [CrossRef]
20. Deng, C.; Gabriel, E.; Skinner, P.; Lee, S.; Barnes, P.; Ma, C.; Gim, J.; Lau, M.L.; Lee, E.; Xiong, H. Origins of Irreversibility in Layered NaNixFeyMnzO$_2$ Cathode Materials for Sodium Ion Batteries. *ACS Appl. Mater. Interfaces* **2020**, *12*, 51397. [CrossRef]
21. Kumar, V.K.; Ghosh, S.; Biswas, S.; Martha, S.K. Practical Realization of O_3-Type $NaNi_{0.5}Mn_{0.3}Co_{0.2}O_2$ Cathodes for Sodium-Ion Batteries. *J. Electrochem. Soc.* **2020**, *167*, 080531. [CrossRef]
22. Yang, Y.; Dang, R.; Wu, K.; Li, Q.; Li, N.; Xiao, X.; Hu, Z. Insights into the Structural Evolution and Sodium Storage Mechanism of P_2-$Na_{2/3}Ni_{1/3}Mn_{2/3}O_2$ Cathode Material. *J. Phys. Chem. C* **2020**, *124*, 1780. [CrossRef]

23. Singh, G.; Acebedo, B.; Cabanas, M.C.; Shanmukaraj, D.; Armand, M.; Rojo, T. Na+ ion conducting gel polymer electrolyte based on poly(vinylidene fluoride-co-hexafluoropropylene) for sodium batteries. *Electrochem. Commun.* **2013**, *37*, 61. [CrossRef]
24. Zhao, J.; Xu, J.; Lee, D.H.; Dimov, N.; Meng, Y.S.; Okada, S. Electrochemical properties of $Na_3V_2(PO_4)_3$/C composite cathode for sodium-ion batteries prepared by a spray-drying method. *J. Power Sources* **2014**, *264*, 235. [CrossRef]
25. Chen, J.; Zou, G.; Deng, W.; Huang, Z.; Gao, X.; Liu, C.; Yin, S.; Liu, H.; Deng, X.; Tian, Y.; et al. Pseudo-Bonding and Electric-Field Harmony for Li-Rich Mn-Based Oxide Cathode. *Adv. Funct. Mater.* **2020**, *30*, 2004302. [CrossRef]
26. Li, Y.; Liang, X.; Chen, G.; Zhong, W.; Deng, Q.; Zheng, F.; Yang, C.; Liu, M.; Hu, J. In-situ constructing $Na_3V_2(PO_4)_2F_3$/carbon nanocubes for fast ion diffusion with high-performance Na^+-storage. *Chem. Eng. J.* **2020**, *387*, 123952. [CrossRef]
27. Wang, P.-F.; Yao, H.-R.; Liu, X.-Y.; Yin, Y.-X.; Zhang, J.-N.; Wen, Y.; Yu, X.; Gu, L.; Guo, Y.-G. Na^+/vacancy disordering promises high-rate Na-ion batteries. *Sci. Adv.* **2018**, *4*, eaar6018. [CrossRef]
28. Kawai, K.; Shi, X.M.; Takenaka, N.; Jang, J.; de Boisse, B.M.; Tsuchimoto, A.; Asakura, D.; Kikkawa, J.; Nakayama, M.; Okubo, M.; et al. Kinetic square scheme in oxygen-redox battery electrodes. *Energy Environ. Sci.* **2022**, *15*, 2591–2600. [CrossRef]
29. Maughan, P.A.; Naden, A.B.; Irvine, J.T.S.; Armstrong, A.R. Manipulating O3/P2 phase ratio in bi-phasic sodium layered oxides via ionic radius control. *Commun. Mater.* **2023**, *4*, 6. [CrossRef]
30. Clément, R.J.; Billaud, J.; Armstrong, A.R.; Singh, G.; Rojo, T.; Bruce, P.G.; Grey, C.P. Large scale computational screening and experimental discovery of novel materials for high temperature CO_2 capture. *Energy Environ. Sci.* **2016**, *9*, 3240. [CrossRef]
31. Das, S.R.; Majumder, S.B.; Katiyar, R.S. Electrochemical properties of $Li/Li_{1-x}Al_xMn_2O_4$ cells. *J. Power Sources* **2005**, *139*, 261. [CrossRef]
32. Yabuuchi, N.; Komaba, S. Recent research progress on iron- and manganese-based positive electrode materials for rechargeable sodium batteries. *Sci. Technol. Adv. Mater.* **2014**, *15*, 043501. [CrossRef] [PubMed]

Disclaimer/Publisher's Note: The statements, opinions and data contained in all publications are solely those of the individual author(s) and contributor(s) and not of MDPI and/or the editor(s). MDPI and/or the editor(s) disclaim responsibility for any injury to people or property resulting from any ideas, methods, instructions or products referred to in the content.